

Spatial modelling of tumour drug resistance: the case of GIST liver metastases

GUILLAUME LEFEBVRE

*Univ. Bordeaux, IMB, UMR 5251 and INRIA
Bordeaux-Sud-Ouest, F-33400, Talence, France*

FRANÇOIS CORNELIS

*Univ. Bordeaux, IMB, UMR 5251, F-33400, Talence, France and Service d'imagerie
diagnostique et interventionnelle de l'adulte, Hopital Pellegrin, CHU de Bordeaux,
Bordeaux, France*

PATRICIO CUMSILLE

*Group of Applied Mathematics (GMA) and Group of Tumour Angiogenesis (GIANT),
Basic Sciences Department, Faculty of Sciences, Universidad del Bio-Bio, Campus
Fernando May, Chillan, Chile and Centre for Biotechnology and Bioengineering,
University of Chile, Beauchef 850, Santiago, Chile*

THIERRY COLIN

*Bordeaux INP, Univ. Bordeaux, IMB, UMR 5251 and INRIA
Bordeaux-Sud-Ouest, F-33400, Talence, France*

AND

CLAIR POIGNARD* AND OLIVIER SAUT

INRIA Bordeaux-Sud-Ouest and CNRS, IMB, UMR 5251, F-33400, Talence, France

*Corresponding author: clair.poignard@inria.fr

[Received on 15 November 2014; revised on 22 September 2015; accepted on 15 January 2016]

This work is devoted to modelling gastrointestinal stromal tumour metastases to the liver, their growth and resistance to therapies. More precisely, resistance to two standard treatments based on tyrosine kinase inhibitors (imatinib and sunitinib) is observed clinically. Using observations from medical images (CT scans), we build a spatial model consisting in a set of non-linear partial differential equations. After calibration of its parameters with clinical data, this model reproduces qualitatively and quantitatively the spatial tumour evolution of one specific patient. Important features of the growth such as the appearance of spatial heterogeneities and the therapeutical failures may be explained by our model. We then investigate numerically the possibility of optimizing the treatment in terms of progression-free survival time and minimum tumour size reachable by varying the dose of the first treatment. We find that according to our model, the progression-free survival time reaches a plateau with respect to this dose. We also demonstrate numerically that the spatial structure of the tumour may provide much more insights on the cancer cell activities than the standard RECIST criteria, which only consists in the measurement of the tumour diameter. Finally, we discuss on the non-predictivity of the model using only CT scans, in the sense that the early behaviour of the lesion is not sufficient to predict the response to the treatment.

Keywords: tumour growth modelling; partial differential equations; cancer; drug resistance; tumour heterogeneity

1. Introduction

Gastrointestinal stromal tumours (GIST) are the most common mesenchymal tumours of the gastrointestinal tract, with an incidence of 9–14 cases per million people per year (see Nilsson *et al.*, 2005). In 25% of cases (see DeMatteo *et al.*, 2000), this type of cancer spreads to the liver. Even though GISTs resist to most of conventional cancer chemotherapies, the discovery of activating mutations of the KIT as well as the role of PDGFR and the new subsequent therapeutic development have revolutionized GISTs treatments. Thanks to the availability of these highly active targeted therapeutic agents, GISTs have become typical models of personalized treatment of cancer (Blay *et al.*, 2012). In particular, the survival of patients with GIST has been improved with the use of tyrosine kinase inhibitors such as imatinib in first-line setting and a multi-targeted receptor tyrosine kinase inhibitor, such as sunitinib or sorafenib, that inhibits PDGFRs, VEGFRs and KIT, as second-line treatment. However, several limitations in terms of diagnosis and outcomes still remain.

First, an important variability exists in the molecular and genetic characteristics that drive the pathogenesis of these tumours. Hirota *et al.* (1998) have proved that molecular alterations in KIT gene with gain-of-function mutations occurred in these tumours (see Hirota *et al.*, 1998). Moreover, in addition to the primary mutation, secondary mutations have been identified in patients with advanced GIST pre-treated with tyrosine kinase inhibitor. At this time, 10 different molecular subsets of GIST with different molecular alterations have been reported. For patients with KIT mutations, an imatinib resistance is frequently observed, as reported in Blay (2011). For other patients, imatinib controls the metastatic disease during a more or less long period, around 20–24 months in 85% of cases. Physicians have then to switch to another molecule or use an alternative therapy. Since the prognosis and the sensitivity to the targeted treatments have been reported to be patient-dependent, we aim at developing a patient-dependent mathematical model based on medical images of liver metastases. We focus on locally advanced GIST in order to determine, for each patient, the time of emergence of mutations in cancer cells, the relapse times after the first-line and the second-line treatments, as well as the geometric features of tumour growth.

Second, the new anti-cancer agents with targeted mechanisms of action as used for the treatment of GIST have demonstrated the inherent limitation and unsuitability of the usual anatomic tumour evaluation, that only considers the largest diameter of the lesion (i.e. the RECIST criteria, see Suzuki *et al.*, 2008). For clinicians, the challenge consists in optimizing these cancer treatments and in particular to determine the more adequate time to switch from the first-line to the second-line treatment, in order to increase the overall survival. The estimate of the relapse time is therefore crucial.

Clinical follow-up to monitor the disease evolution is mainly performed with CT scans. We emphasize that the effect of these new drugs changes the paradigm according to which the tumour sensitivity to the treatment is measured (see Schramm *et al.*, 2013), since CT scans have reported other information such as tumour heterogeneity: the RECIST criteria seems no more sufficient.

The aim of this work is to provide a spatial model of standard treated GISTs in order to compare the model with the images and possibly to highlight the peculiarities of the tumour growth or regrowth. It is worth noting that this article is a first step in the modelling of tumour drug resistance based on clinical images.

We provide a model, which consists in a non-linear system of partial differential equations (PDEs), in order to account for the spatial aspect of the tumour growth. Currently, the models based on ordinary differential equations as the models of Mendelsohn, Gompertz or Bertalanffy make it possible to track the tumour area growth but they do not consider the spatial aspects of the growth. We refer to the review by Benzekry *et al.* (2014) for more details on such one-dimensional models Benzekry *et al.* (2014). Our model is derived in the same vein as Ribba *et al.* (2006) — we also refer to Colin *et al.* (2012,

2014) — in order to describe the evolution of the disease. The main novelty of the model lies in the description of the treatments. Two treatments are considered: the first treatment consists in a cytotoxic effect while the second-line treatment has both cytotoxic and anti-angiogenic effects. Three different proliferative cells are used to describe the resistance to treatments: one cell population is sensitive to the two treatments, another one is only sensitive to the second treatment while the third cell population is resistant to both treatments. We also provide a simple model of angiogenesis, which is crucial in the metastasis growth.

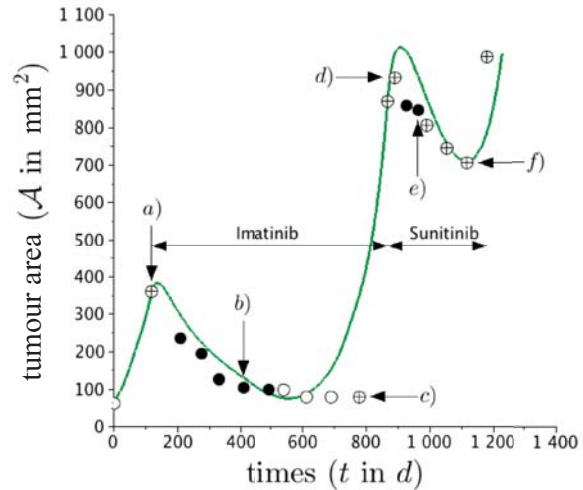
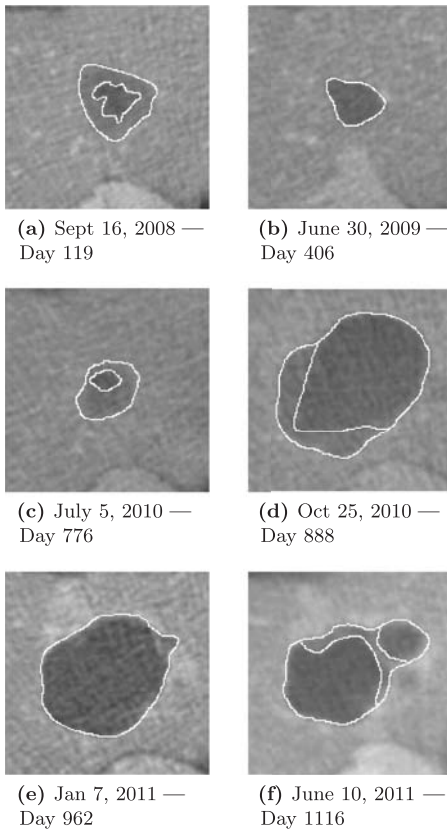
Once the model is built, we provide an appropriate numerical scheme that makes it possible to solve the PDEs. In particular, we present in Section 3 a new WENO5-type scheme that stabilizes the computation by using a combination of the classical WENO5 stencil and a twisted stencil. We then extensively compare our model to the clinical data of one specific patient, for whom we have the whole clinical protocol, in Section 4. Let us mention that it has been necessary to introduce a numerical reconstitution of the CT scan from the numerical results, in order to compare the grey levels of CT scans with our simulations. Once the fitting has been obtained, we then investigate numerically the effect of the treatment dose on the tumour growth progression. The counter-intuitive result lies in the fact that according to the parameters we use for the fitting with the data, the increase of the dose of the first treatment does not improve the progression-free survival time. This result is explained in Subsection 4.2.2. We then conclude on the consistency of our model by presenting the different behaviours of the tumour evolution that can be obtained. We also numerically fit the tumour area with another patient, whose tumour is close to the liver boundary. It is worth noting that for such patients, the shape of the tumour cannot be recovered. Our model does not take the corresponding mechanical constraints into account. However, the tumour area seems to be well reproduced by our simulations. This article is a first step for a better understanding of the tumour drug resistance of GIST metastases to the liver. However, as we mention in the conclusion, CT scans do not provide enough information to make our model predictive. This is due to the fact that, based on CT scans, it is impossible to evaluate the quantity of cells that are not sensitive to the second-line treatment. Therefore, even if we can find parameters that fit with the tumour evolution at its early stage and during the first-line treatment, we cannot predict the long-term behaviour, after the second-line treatment. We are confident that data concerning the structure of the tumour, such as data arising from functional imaging, should help in improving such predictivity of the model.

1.1 *Main Insights*

On the left part of Fig. 1, we provide the sequence of the CT scans, and on the right part, we give the tumour area evolution of the GIST liver metastasis of one specific patient called Patient A. On each CT scan of Patient A, we have depicted the darkest region, which corresponds mainly to the necrotic cells. During the tumour evolution, one can see that the heterogeneity of the tumour changes (for instance in Fig. 1(b), the tumour is homogeneous, while in Fig. 1(f) is heterogeneous). We distinguish in the tumour area evolution the points corresponding to a homogeneous tumour (in fulfilled circle) from the point corresponding to heterogeneous tumour.

Interestingly, just before the tumour regrowth at Day 776 (Fig. 1(c)) and Day 1116 (Fig. 1(f)), one can see on the tumour a rim clearer than the dark core, while the response to the treatment is followed by a darkening of the tumour (see Fig. 1(b) and (e)). Such successive stages of tumour homogeneities/heterogeneities, are particularly pronounced in GIST liver metastases, and our goal is to provide an explanation of such behaviour.

The first result of this article lies in the fact that it makes it possible to describe the tumour evolution in terms of tumour area compared with the CT scans measurements, as presented by Fig. 1(g): the



(g) Tumour area. Each point represents the tumour area measured on CT scans and the line stands for our numerical results. The letter refers to the CT scans shown on the left. The symbol \oplus stands for heterogeneous tumour, \bullet stands for rather homogeneous tumour and \circ stands for CT scan on which it is difficult to detect heterogeneous aspect. The value of parameters used in the numerical simulation is given in Table 2.

FIG. 1. Spatial evolution of the liver metastasis of Patient A on a series of CT scans.

continuous line corresponds to the numerical results. It is worth noting that we do not provide a one-dimensional model that describes the tumour volume. We deal with a complex non-linear PDE model, which is phenomenological and which describes the behaviour of cancer cells with respect to the space and the time variables. Therefore, this first fit with the tumour area is a non-trivial insight.

The second main insight is that our model brings new information on the tumour structure, that seems corroborated with the CT scans. Actually, as it will be presented in the following, we link the tumour heterogeneity to an increase in the cellular activity, meaning that a resistant phenotype is emerging in the clearer region. According to our modelling, such a behaviour can be seen before the treatment failure, while RECIST criteria has not changed. For instance in Fig. 2, we compare the structure of the tumour at two different days: the heterogeneity of the tumours seems to be well captured by the numerical simulations. Therefore, our article can be seen as a first step in developing new tools to evaluate the tumour response to treatment based on tyrosine kinase inhibitors.

2. Description of the model

Our model is a system of PDEs similar to the model of Bresch *et al.* (2010). Roughly, the tumour is described thanks to densities of proliferative and necrotic cancer cells denoted by P and N , respectively. Cell proliferation causes an increase of pressure that implies a transport of the surrounding cells that leads

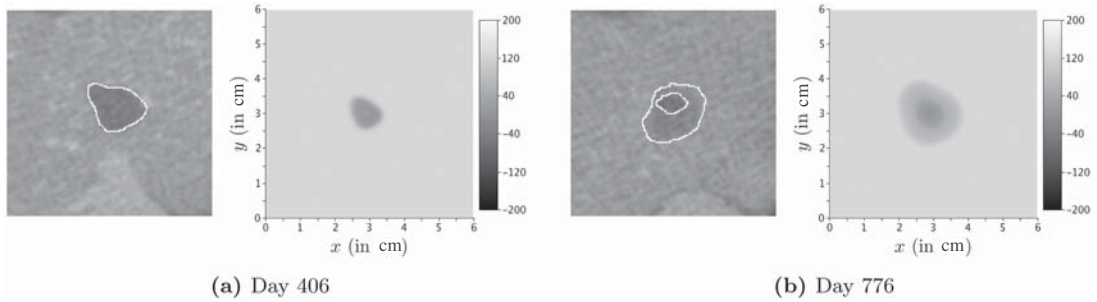


FIG. 2. Comparison between CT scans of Patient A and the numerical simulations.

 TABLE 1 List of quantities computed by the model – $d = \text{day}$

Name	Meaning	Unit
$P_1(t, \mathbf{x})$	Fraction of cancer cells that are both sensitive to treatments \mathcal{T}_1 and \mathcal{T}_2	—
$P_2(t, \mathbf{x})$	Fraction of cancer cells that are resistant to \mathcal{T}_1 and sensitive to \mathcal{T}_2	—
$P_3(t, \mathbf{x})$	Fraction of cancer cells that are both resistant to treatments \mathcal{T}_1 and \mathcal{T}_2	—
$P(t, \mathbf{x})$	Fraction of proliferative cancer cells (equal to $P_1 + P_2 + P_3$)	—
$N(t, \mathbf{x})$	Fraction of necrotic cells	—
$S(t, \mathbf{x})$	Fraction of healthy cells	—
$M(t, \mathbf{x})$	Fraction of nutrients // Vascularization	—
$\xi(t)$	Average velocity of nutrients transport in direction of the tumour	cm.d^{-1}
$\mathbf{v}(t, \mathbf{x})$	Velocity of the passive movement of the tumour under the pressure	cm.d^{-1}
$\Pi(t, \mathbf{x})$	Medium pressure ^a	$\text{kg.cm}^{-1}.\text{d}^{-2}$

^aThe mass unit in the pressure Π and in the permeability k has no importance, since only $k\nabla\Pi$ is relevant, and this term is homogeneous to cm.d^{-1} . Thus, k and Π have just to be in the same arbitrary mass unit.

to an increase of the tumour volume. The cells located at the centre of the tumour turn into a necrotic phase, because of a lack of oxygen for instance, except if angiogenesis has occurred to provide them nutrient supply. Angiogenesis and nutrient supply are taken into account in our model with a simplistic description similar to Billy *et al.* (2009), Saut *et al.* (2014): since the vascularization drives the nutrient concentration towards the tumour, we introduce a variable M that describes both vascularization, neovascularization and nutrients brought to the tumour thanks to an advection-diffusion equation. We also introduce growth factor effects through a variable ξ that modulates M . The set of quantities used in our model is resumed in Table 1.

The main novelty lies in the modelling of the treatments. Two treatments are considered (one can see in Lorz *et al.* (2013), the recent works by Lorz *et al.* for more elaborated models on drug resistance). The first one is a specific tyrosine kinase inhibitor, such as imatinib, that has a cytotoxic effect on proliferative cells. The second treatment is a multi-targeted kinase inhibitor, such as sunitinib or sorafenib, that has both cytotoxic and anti-angiogenic effects. In addition to the cytotoxic effect, it blocks the production of growth factors such as vascular endothelial growth factors and thus decreases the nutrient supply brought to the tumour. It is well known that the cytotoxic drugs do not impact similarly all the metastatic cancer cells since resistant phenotype can appear in the proliferative cell population. Moreover, cancer cells can resist differently to hypoxia. Therefore we split, as in Bresch *et al.* (2009), the density P of proliferative cells (P cells) into three subpopulations P_1 , P_2 and P_3 , such that $P = P_1 + P_2 + P_3$, where

- P_1 denotes the fraction of proliferative cells that are sensitive to the first-line treatment \mathcal{T}_1 , based on imatinib molecule and also to the second-line treatment \mathcal{T}_2 , based on sunitinib or sorafenib, that has both cytotoxic and anti-angiogenic effect,
- P_2 describes the density of proliferative cells that are resistant to the first-line treatment \mathcal{T}_1 and sensitive to treatment \mathcal{T}_2 ,
- P_3 stands for proliferative cells that are resistant to both treatments.

It is worth noting that we do not aim at describing the evolution of the tumour from the very beginning of the GIST, but we only focus on the evolution of the metastasis located at the liver. Therefore, according to the clinical observations, it seems relevant to consider that the three cell subpopulations are present when the GIST metastasis is detected.

2.1 The mathematical model

Let Ω be the domain of interest, where the tumour grows, and denote by $\partial\Omega$ its boundary, which is supposed as regular as needed. The domain Ω is assumed to be strictly embedded in a tissue — the liver — which is much larger. In addition, we assume that the tumour does not reach the boundary $\partial\Omega$.

2.1.1 PDEs on proliferative, necrotic and healthy cells. The proliferative cell densities are driven by the following transport equations:

$$\partial_t P_1 + \nabla \cdot (\mathbf{v}P_1) = (\gamma_{pp}(M) - \gamma_{pd}(M))P_1 - (\mu_1 \chi_1(t) + \mu_2 \chi_2(t))(1 + M)P_1 \quad \text{in } \Omega, \quad (2.1)$$

$$\partial_t P_2 + \nabla \cdot (\mathbf{v}P_2) = (\gamma_{pp}(M) - \gamma_{pd}(M))P_2 - \mu_2 \chi_2(t)(1 + M)P_2 \quad \text{in } \Omega, \quad (2.2)$$

$$\partial_t P_3 + \nabla \cdot (\mathbf{v}P_3) = (\gamma_{pp}(M) - \gamma_{pd}(M))P_3 \quad \text{in } \Omega, \quad (2.3)$$

where $\chi_i(t) = \mathbb{1}_{[\mathcal{T}_{ini}^i, \mathcal{T}_{end}^i]}(t)$ is the time-characteristic functions of treatment \mathcal{T}_i and μ_i stands for the rate of the death¹ due to \mathcal{T}_i of the proliferative cells, for $i \in \{1, 2\}$. The term $\mathbf{v}(t, \mathbf{x})$ denotes the velocity involved in the tumour area changes and $M(t, \mathbf{x})$ stands for the vascularization and the nutrient supply. The rate of proliferation (resp. death) of P cells, denoted by γ_{pp} (resp. γ_{pd}), depends on M as follows:

$$\gamma_{pp}(M) = \gamma_0 \frac{1 + \tanh(R(M - M_{th}))}{2}, \quad (2.4)$$

$$\gamma_{pd}(M) = \gamma_1 \frac{1 - \tanh(R(M - M_{th}))}{2}, \quad (2.5)$$

where R is a numerical smoothing parameter², γ_0 and γ_1 are, respectively, proliferative/decay parameters and M_{th} is the hypoxia threshold.

¹The death rate due to the treatment is clearly linked to the dose of drug delivered to the patient, but not only. For instance, the sensitivity of the patient and the dose that really reaches the tumour are also involved.

²Note that the functions γ_{pp} and γ_{pd} are merely regularized Heaviside functions. For the numerical simulations, we arbitrarily set R to 5.

We assume that healthy cells are only sensitive to hypoxia, and they are passively transported by the tumour area changes:

$$\partial_t S + \nabla \cdot (\mathbf{v}S) = -\gamma_{sd}(M)S, \quad (2.6)$$

where γ_{sd} is the rate of death of healthy cells due to hypoxia:

$$\gamma_{sd}(M) = C_S \gamma_1 \max\left(0, -\tanh\left(R(M - M_{th})\right)\right). \quad (2.7)$$

Note that γ_{sd} vanishes exactly if $M \geq M_{th}$ in order to ensure that the $S = 1$ on the outer boundary at any time. Finally, necrotic cell density satisfies

$$\partial_t N + \nabla \cdot (\mathbf{v}N) = \gamma_{pd}(M)P + \gamma_{sd}(M)S + (\mu_1 \chi_1(t)P_1 + \mu_2 \chi_2(t)(P_1 + P_2))(1 + M) - \delta(1 + M)N, \quad (2.8)$$

where

$$P = P_1 + P_2 + P_3, \quad (2.9)$$

and δ is a parameter that controls the elimination rate of the necrotics cells by the immune system.

The following Dirichlet conditions are used on the boundary if the velocity is incoming:

$$P_1 = P_2 = P_3 = N = 1 - S = 0 \quad \text{for } \mathbf{x} \in \partial\Omega, \text{ if } \mathbf{v} \cdot \mathbf{n} < 0, \quad (2.10)$$

where \mathbf{n} is the outgoing normal vector of the domain Ω .

2.1.2 Mechanics. Note that in the above equations, we have used the same velocity for all the cell species. This assumption would be probably inappropriate for primary tumours since it is known that some cells can have an infiltrative behaviour. Therefore, for primary tumours, several velocities have to be used as in [Byrne & Preziosi \(2003\)](#). However, for metastases, the situation is quite different. Indeed, the movement of the tumour front is mainly due to the increase of volume that is induced by the proliferation. Migration effects can be neglected for metastases. The simplest way to describe this phenomenon is therefore to use only one velocity that account for the displacement induced by the change of volume and then to impose the following saturation condition (as in [Ambrosi & Preziosi \(2002\)](#))

$$P + N + S = 1. \quad (2.11)$$

Summing (2.1),(2.2),(2.3),(2.6) and (2.8), we obtain

$$\nabla \cdot \mathbf{v} = \gamma_{pp}P - \delta(1 + M)N. \quad (2.12)$$

As it is well known in continuous mechanics, the divergence of the velocity is the rate of change of the volume, therefore, equation (2.12) describes exactly the fact that the increase of volume is the only source of movement. However, at this point, the system is not closed and the simplest closure relation is Darcy's law as in [Ribba et al. \(2006\)](#):

$$\begin{cases} \mathbf{v}(t, \mathbf{x}) = -k\nabla\Pi(t, \mathbf{x}) & \text{in } \Omega, \\ \Pi(t, \mathbf{x}) = 0 & \text{on } \partial\Omega, \end{cases} \quad (2.13)$$

where Π is the pressure (or potential) of the medium and k its permeability. Of course Stokes' law or any viscoelastic model could be used, we refer to [Bresch et al. \(2009\)](#) and [Ambrosi & Preziosi \(2002\)](#); [Byrne & Preziosi \(2003\)](#) for more details. Such more complicated models can provide better descriptions of the tumour from the mechanical point of view. However, in order to be able to fit the medical data, we intend to keep the complexity of the model as low as possible. It seems not realistic to decide the rheological properties of the tumour from medical images. We therefore choose to use the simplest framework for the mechanical properties.

The homogeneous Dirichlet condition in (2.13) states that outside Ω , the pressure of the healthy tissue is not affected by the gradient of pressure generated by the tumour growth. Of course, this assumption will not be valid for huge tumours, which may impact the shape of the liver. In other words, we assume that the tumour is not mechanically constrained by the extratumoural region.

2.1.3 Vascularization, nutrient supply and angiogenesis. It remains to describe the vascularization/nutrient supply M and the impact of treatment \mathcal{T}_2 on it. It is worth noting that the second-line treatment does not impact directly M , but it blocks the production of growth factors that drive the quantity M .

We thus introduce a scalar variable ξ , which is related to the mean concentration of endothelial growth factors produced by cancer cells. It has been reported by [Holmes et al. \(2007\)](#) that hypoxic cells increase their production of growth factors, while highly proliferative cells do not need additional nutrient supply. Therefore, if M is below the threshold M_{th} then ξ should increase. Note also that the anti-angiogenic effect of treatment \mathcal{T}_2 decreases the production of ξ , but only for the cells P_1 and P_2 since P_3 is the density of cells that are sensitive neither to \mathcal{T}_1 nor to \mathcal{T}_2 . We thus describe the evolution of ξ as

$$\partial_t \xi = \alpha \int_{\Omega} (1 + \epsilon_{\xi} - \gamma_{\text{pp}}(M)/\gamma_0) \left((1 - \nu_2 \chi_2(t))(P_1 + P_2) + P_3 \right) dx - \lambda \xi. \quad (2.14)$$

The dimensionless parameter $\nu_2 \in (0, 1)$ stands for the anti-angiogenic effect of \mathcal{T}_2 , assumed to be similar for P_1 and P_2 , while ϵ_{ξ} reflects the ground production of growth factors by cancer cells.

Let us recall that since the nutrients are supplied to the tumour by the vascularization, we choose to use only one unknown to describe the variation of the amount of nutrients and the vascularization, in order to keep the complexity of the model as low as possible. We call M this quantity. We use a transport-reaction-diffusion equation to describe its evolution:

$$\begin{cases} \partial_t M - \xi \frac{\nabla S}{\|\nabla S\|} \cdot \nabla M = C_0 S \left(1 - \frac{M}{2M_{\text{th}}} \right) - \eta PM + \psi \Delta M & \text{in } \Omega, \\ M(t, \mathbf{x}) = 2M_{\text{th}} & \text{on } \partial\Omega, \end{cases} \quad (2.15)$$

where C_0 is the angiogenic capacity of healthy cells, η denotes the rate of nutrients consumption and ψ is a diffusion parameter. The neovasculature is brought to the tumour from the healthy tissue, which is assumed to be well vascularized. The transport term $\xi \frac{\nabla S}{\|\nabla S\|} \cdot \nabla M$ of equation (2.15) accounts for this phenomenon. The intensity of this transport term equals ξ , which is linked to the total endothelial growth factor produced by the proliferative cancer cells. It is the way we express that the amount of new blood vessels in the tumour is directly correlated to the concentration of endothelial growth factor. The diffusive term describes the diffusion of the nutrients into the tumour. From the numerical point of view, this term has a regularizing effect on the vascularization M and thus stabilizes the numerical model. The term

$-\eta PM$ stands for the consumption of nutrients by the tumour, while $C_0 S \left(1 - \frac{M}{2M_{th}}\right)$ is a saturated source term in the healthy tissue. Note that if we have initially

$$0 \leq \|M|_{t=0}\|_{L^\infty} \leq 2M_{th}, \tag{2.16}$$

then at any time t , $0 \leq M(t) \leq 2M_{th}$. This reflects the fact that the healthy tissue surrounding the tumour is well vascularized and supplied with enough nutrients.

2.2 Vector formulation of the equations on cancer cells

To simplify the notations, let us denote the vector of cell populations by $\mathbf{W} = (P_1, P_2, P_3, N)$. We define the vector function

$$\mathbf{G}(M, \mathbf{W}) = \begin{pmatrix} (\gamma_{pp}(M) - \gamma_{pd}(M) - (\mu_1 \chi_1(t) + \mu_2 \chi_2(t))(1+M))P_1 \\ (\gamma_{pp}(M) - \gamma_{pd}(M) - \mu_2 \chi_2(t)(1+M))P_2 \\ (\gamma_{pp}(M) - \gamma_{pd}(M))P_3 \\ \gamma_{pd}(M)P + \gamma_{sd}(M)(1-P-N) + (\mu_1 \chi_1 P_1 + \mu_2 \chi_2 (P_1 + P_2))(1+M) - \delta(1+M)N \end{pmatrix}.$$

It is also convenient to define $F(M, \mathbf{W})$ as

$$F(M, \mathbf{W}) := \gamma_{pp}(M) \sum_{i=1}^3 W_i - \delta(1+M)W_4, \tag{2.17}$$

so that the set of equations (2.1)–(2.3) and (2.8) and (2.12) closed by the Darcy law read

$$\begin{cases} \partial_t \mathbf{W} + (\nabla \mathbf{W}) \cdot \mathbf{v} + \mathbf{W}(\nabla \cdot \mathbf{v}) = \mathbf{G}(M, \mathbf{W}) & \text{on } \Omega, \\ \mathbf{W} = 0 & \text{on } \partial\Omega, \text{ if } \mathbf{v} \cdot \mathbf{n} < 0, \end{cases} \tag{2.18}$$

and

$$\begin{cases} -\nabla \cdot (k \nabla \Pi) = F(M, \mathbf{W}), & \text{in } \Omega, \\ \Pi(t, \mathbf{x}) = 0 & \text{on } \partial\Omega. \end{cases} \tag{2.19}$$

Note that the density of healthy cells S is then given by (2.11).

3. Numerical methods

We use a two-dimensional cartesian staggered grid with a finite volume method. For the numerical calculations, the domain Ω is the rectangle $[0, L] \times [0, D]$. The domain is meshed by a cartesian grid with N_x points along the x -axis and N_y points along the y -axis.

The cancer cell densities are discretized at the centre of the cell grid and the velocities are discretized at the middle of each edge as shown in Fig. 3.

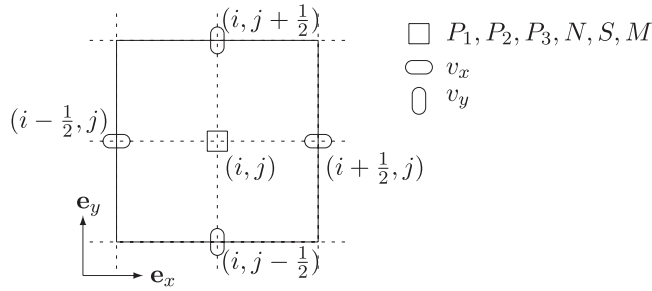


FIG. 3. Discretization of unknown variables on one cell grid.

Note that the equality (2.11) gives straightforwardly S , without solving equation (2.6). We split the computation into the following steps.

- Given³ \mathbf{W}^n , and M^n at the time t^n , we infer $F^n = F(M^n, \mathbf{W}^n)$ and $\mathbf{G}^n = \mathbf{G}(M^n, \mathbf{W}^n)$.
- We first compute the pressure Π^n solution to (2.19) with F^n as right hand side, from which we infer the velocity \mathbf{v}^n thanks to the equation (2.13).
- Then the new computation time $t^{n+1} = t^n + \Delta t$ is determined using the equation (3.17).
- Afterwards we compute \mathbf{W}^{n+1} from (2.18), from which we infer S^{n+1} .
- We end by computing ξ^{n+1} and M^{n+1} thanks to (2.14)–(2.15).

Let present precisely the schemes used in the numerical simulations.

3.1 Computation of pressure and velocity

According to (2.12) and (2.13), the pressure Π^n is given by

$$\begin{cases} -\nabla \cdot (k \nabla \Pi^n) = F^n := F(M^n, \mathbf{W}^n) & \text{on } \Omega, \\ \Pi^n = 0 & \text{on } \partial\Omega, \end{cases} \quad (3.1)$$

where F is defined by (2.17). We solve this equation thanks to a classical five-points scheme. The component along \mathbf{e}_x of the velocity $v_{i+1/2,j}^{x,n}$ at $\mathbf{x}_{i+1/2,j}$ (resp. the component along \mathbf{e}_y , $v_{i,j+1/2}^{y,n}$ at the point $\mathbf{x}_{i,j+1/2}$) are given thanks to

$$v_{i+1/2,j}^{x,n} = -k \frac{\Pi_{i+1,j}^n - \Pi_{i,j}^n}{\Delta x}, \quad v_{i,j+1/2}^{y,n} = -k \frac{\Pi_{i,j+1}^n - \Pi_{i,j}^n}{\Delta y}$$

and the velocity \mathbf{v}_{ij}^n at the point \mathbf{x}_{ij} is approached by

$$\mathbf{v}_{ij}^n = v_{ij}^{x,n} \mathbf{e}_x + v_{ij}^{y,n} \mathbf{e}_y = \frac{1}{2} (v_{i+1/2,j}^{x,n} + v_{i-1/2,j}^{x,n}) \mathbf{e}_x + \frac{1}{2} (v_{i,j+1/2}^{y,n} + v_{i,j-1/2}^{y,n}) \mathbf{e}_y. \quad (3.2)$$

³The superscript n stands for the discrete time t^n of the quantity (for instance, S^n is the density of healthy cells at the time t^n)

3.2 Advection equation

By definition of \mathbf{F} given by (2.17), the equation (2.12) leads to $\nabla \cdot \mathbf{v} = \mathbf{F}$. Thus, the equation (2.18) can read also as a non-conservative form

$$\partial_t \mathbf{W} + (\nabla \mathbf{W}) \cdot \mathbf{v} = \mathbf{G}(\mathbf{M}, \mathbf{W}) - (\nabla \cdot \mathbf{v}) \mathbf{W} = \mathbf{G}(\mathbf{M}, \mathbf{W}) - \mathbf{F}(\mathbf{M}, \mathbf{W}) \mathbf{W}, \quad (3.3)$$

solved thanks to the following time-splitting scheme

$$\frac{\mathbf{W}^* - \mathbf{W}^n}{\Delta t/2} = \mathbf{G}^n - \mathbf{F}^n \mathbf{W}^n, \quad (3.4)$$

$$\frac{\mathbf{W}^\# - \mathbf{W}^*}{\Delta t} + (\nabla \mathbf{W}^*) \cdot \mathbf{v}^n = 0, \quad (3.5)$$

$$\frac{\mathbf{W}^{n+1} - \mathbf{W}^\#}{\Delta t/2} = \mathbf{G}^n - \mathbf{F}^n \mathbf{W}^n. \quad (3.6)$$

This non-conservative form is chosen in order to use the information that we already have on the divergence of the velocity, thanks to equality (2.12).

A WENO5-type method as given by Liu *et al.* (1994) is used to approach the gradient $\nabla \mathbf{W}$ involved in (3.5). As we will see below, the initial data (4.7)–(4.8) for the densities of cells are smooth. It therefore makes sense to use a WENO5-type scheme in order to decrease the numerical diffusion.

3.3 Computation of the quantities ξ and M

The scalar equation (2.14) is solved thanks to the classical forward Euler method:

$$\frac{\xi^{n+1} - \xi^n}{\Delta t} = \alpha \int_{\Omega} (1 + \epsilon_\xi - \gamma_{pp}(M^n)/\gamma_0) \left((P_1^n + P_2^n)(1 - \nu_2 \chi_2(t^n)) + P_3^n \right) d\mathbf{x} - \lambda \xi^n, \quad (3.7)$$

where we use a standard rectangle rule to approach the integral in the right hand side.

In order to solve the advection-diffusion equation (2.15) satisfied by M , we use the following time-splitting schemes:

$$\frac{M^* - M^n}{\Delta t/2} = C_0 S^n \left(1 - \frac{M^n}{2M_{th}} \right) - \eta P^n M^n, \quad (3.8)$$

$$\frac{M^\# - M^*}{\Delta t} - \psi \frac{\Delta M^\# + \Delta M^*}{2} = \xi^n \frac{\nabla S^n}{\|\nabla S^n\|} \nabla M^n, \quad (3.9)$$

$$\frac{M^{n+1} - M^\#}{\Delta t/2} = C_0 S^n \left(1 - \frac{M^n}{2M_{th}} \right) - \eta P^n M^n. \quad (3.10)$$

Equation (3.9) is computed as a heat diffusion equation with a standard five-points scheme on the grid. The right-hand side is approached by a WENO5-type scheme.

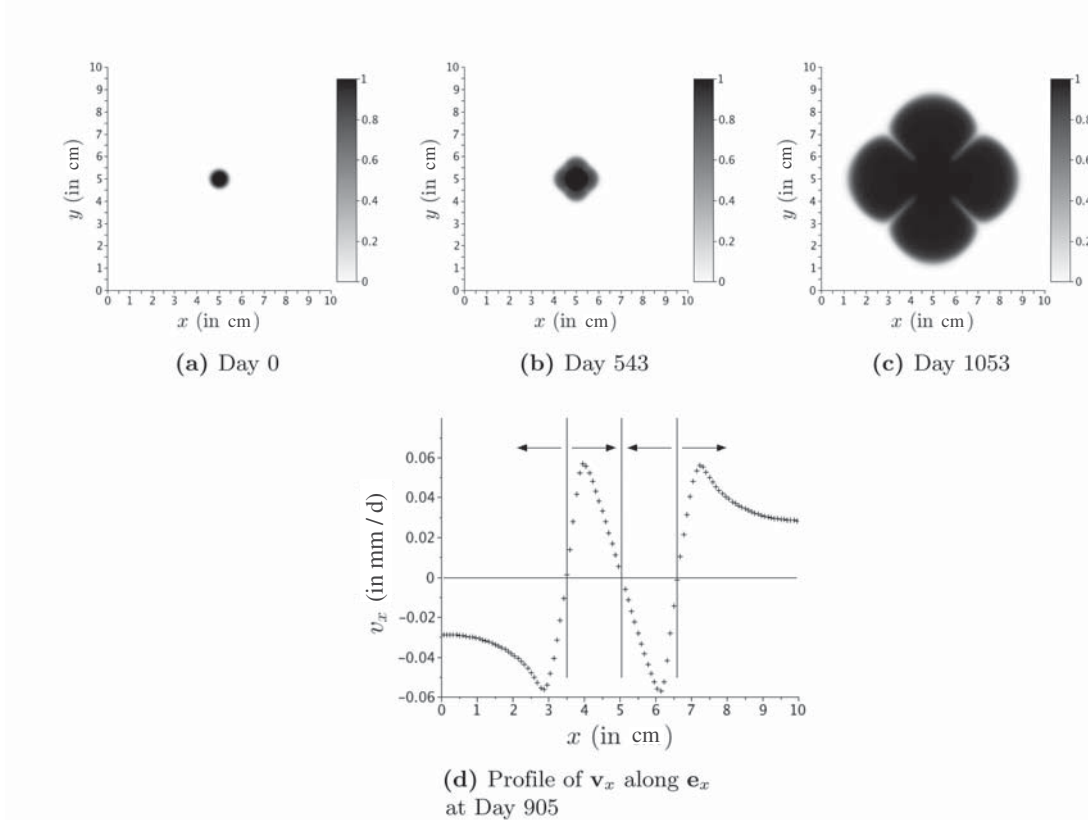


FIG. 4. Numerical simulations with the standard WENO5 stencil for the specific set of parameters. Starting from circular initial data, clover-like structures appear.

3.4 The twin-WENO5: a modified WENO5 scheme

The standard WENO5 scheme as given by Liu *et al.* (1994) is accurate in most of the cases; however, some sets of parameters⁴ make us face numerical instabilities. Note that such instabilities were also produced with classical upwind scheme. More precisely, starting from irrotational initial data, the simulation can generate a clover-like structure, as reported by Fig. 4, while the circular shape should be preserved.

Note that such errors on the shape provide error on the evolution of the area of the lesion, since the clover shape increases the contact surface and thus modifies the interaction between the vascularization and the tumour. These instabilities have to be fixed. The problem is due to the WENO5 stencil that tends to favour the directions of the grid where changes in the velocity direction occur. As we can see on Fig. 4(d), on the centre of the tumour (around $x = 5$ cm in Fig. 4d), there is a compression point: the velocity has centripetal directions, since v_x is positive on the right and negative on the left. Moreover,

⁴The set of parameters has been found incidently by fitting the tumour area evolution of Patient B, see Section 5.1.

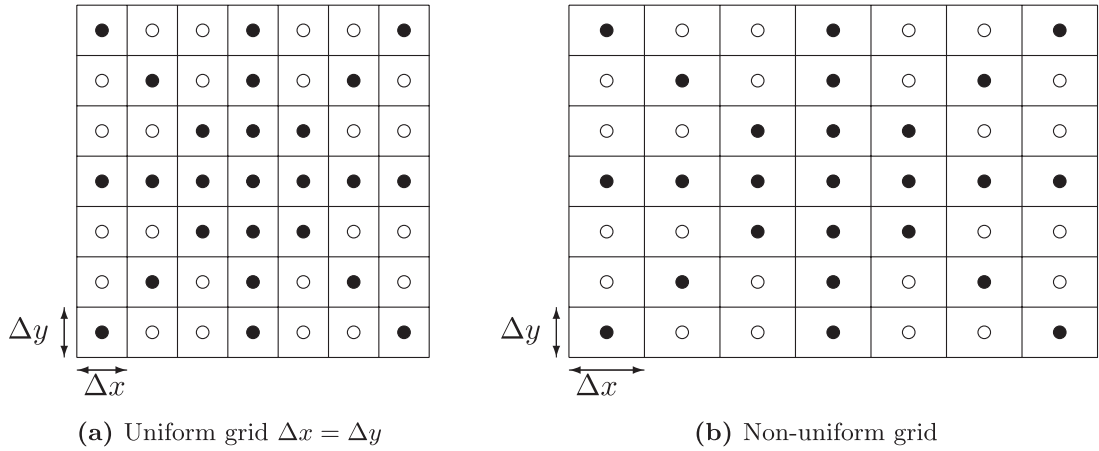


FIG. 5. Stencil of the twin-WENO5 scheme for a uniform grid (left) and a non-uniform grid (right).

around 1.5 cm from the centre of the tumour, there is a rim of proliferative cells that induce a spreading movement: the velocity is centripetal close to the centre but centrifugal far from it.

More precisely, for the standard WENO5 scheme, at any point \mathbf{x}_{ij} of the grid, the numerical approximation \mathbf{W}_{ij}^{n+1} to equation (3.5) at the time t^{n+1} is given by

$$\mathbf{W}_{ij}^{n+1} = \mathbf{W}_{ij}^n + \Delta t \left(v_{ij}^{x,n} \mathcal{F}(\Delta x, (\mathbf{W}_{i+k,j}^n)_{k=-3,\dots,3}) + v_{ij}^{y,n} \mathcal{F}(\Delta y, (\mathbf{W}_{i,j+k}^n)_{k=-3,\dots,3}) \right), \quad (3.11)$$

where $v_{ij}^{x,n}$ and $v_{ij}^{y,n}$ are defined by (3.2) and where \mathcal{F} is the WENO5 functional given by Liu *et al.* (1994). In order to avoid the numerical instabilities, we introduce the following twin-WENO5 scheme, which is a combination of the standard WENO5 stencil and a rotation at the angle α of the WENO5 stencil (see Fig. 5), where α is defined by the grid steps Δx and Δy as

$$\alpha = \arctan(\Delta y / \Delta x) \in (0, \pi/2).$$

We introduce the coefficients $(v_{ij}^{r,n}, v_{ij}^{\theta,n})$ and Δr defined by⁵

$$\begin{pmatrix} v_{ij}^{r,n} \\ v_{ij}^{\theta,n} \end{pmatrix} = \begin{pmatrix} \cos \alpha & \sin \alpha \\ -\sin \alpha & \cos \alpha \end{pmatrix} \begin{pmatrix} v_{ij}^{x,n} \\ v_{ij}^{y,n} \end{pmatrix}, \quad \Delta r = \sqrt{\Delta x^2 + \Delta y^2}, \quad (3.12)$$

and we discretize equation (3.5) thanks to our twin-WENO5 scheme:

$$\begin{aligned} \mathbf{W}_{ij}^{n+1} = & \mathbf{W}_{ij}^n + (1 - \beta) \Delta t \left(v_{ij}^{x,n} \mathcal{F}(\Delta x, (\mathbf{W}_{i+k,j}^n)_{k=-3,\dots,3}) + v_{ij}^{y,n} \mathcal{F}(\Delta y, (\mathbf{W}_{i,j+k}^n)_{k=-3,\dots,3}) \right) \\ & + \beta \Delta t \left(v_{ij}^{r,n} \mathcal{F}(\Delta r, (\mathbf{W}_{i+k,j+k}^n)_{k=-3,\dots,3}) + v_{ij}^{\theta,n} \mathcal{F}(\Delta r, (\mathbf{W}_{i-k,j+k}^n)_{k=-3,\dots,3}) \right), \end{aligned} \quad (3.13)$$

⁵The coefficients $v_{ij}^{r,n}$ and $v_{ij}^{\theta,n}$ are defined such that

$$\mathbf{v}_{ij}^n = v_{ij}^{x,n} \mathbf{e}_x + v_{ij}^{y,n} \mathbf{e}_y = v_{ij}^{r,n} \mathbf{e}_r + v_{ij}^{\theta,n} \mathbf{e}_\theta, \quad \text{with} \quad \mathbf{e}_r = \cos \alpha \mathbf{e}_x + \sin \alpha \mathbf{e}_y, \quad \mathbf{e}_\theta = -\sin \alpha \mathbf{e}_x + \cos \alpha \mathbf{e}_y.$$

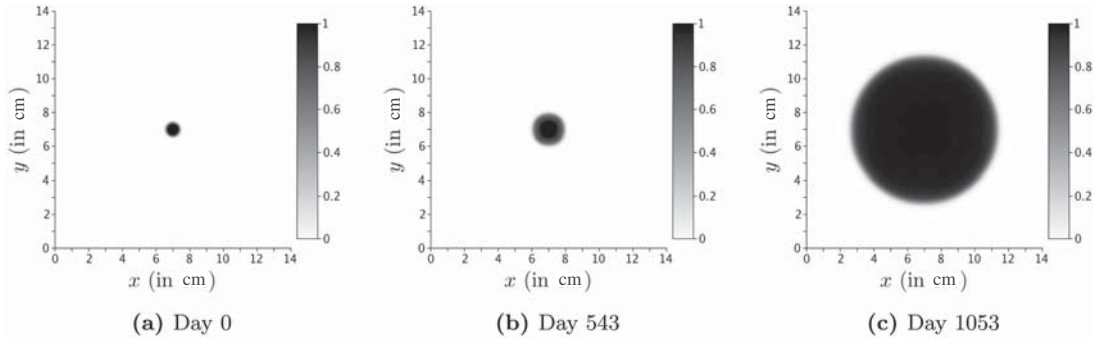


FIG. 6. Numerical simulations with the twin-WENO5 scheme ($\beta = 0.26$). Comparing in Fig. 4, the conservation of irrotational invariance is very clearly improved.

where $\beta \in (0, 1)$ is a numerical parameter that has to be chosen. In particular, the standard WENO5 scheme holds for $\beta = 0$. As we can see on Fig. 6, our new scheme keeps the irrotational property in cases where WENO5 does not.

3.5 CFL condition

In addition, CFL-type restriction condition is required to preserve numerical stability. First, the WENO5-type scheme leads to a CFL condition that writes :

$$\Delta t < \min \left(\frac{\Delta x}{\max |v_x|}, \frac{\Delta y}{\max |v_y|}, \frac{\min(\Delta x, \Delta y)}{\xi} \right) := \Delta t_{\text{adv}}. \quad (3.14)$$

The forward Euler scheme on equation (3.4) leads to the following inequality (coordinate by coordinate)

$$\mathbf{W}^* = \mathbf{W}^n + \frac{\Delta t}{2} (\mathbf{G}^n - \mathbf{F}^n \mathbf{W}^n) \geq \left(\mathbf{1} + \frac{\Delta t}{2} (\bar{\mathbf{G}}^n - \mathbf{F}^n \mathbf{1}) \right) \circ \mathbf{W}^n,$$

where $\mathbf{1} = (1, 1, 1, 1)$, the symbol \circ stands for the Hadamard product (the pointwise product of the vectors, coordinate by coordinate) and where $\bar{\mathbf{G}}^n$ reads:

$$\bar{\mathbf{G}}^n = \begin{pmatrix} \gamma_{\text{pp}}(M^n) - \gamma_{\text{pd}}(M^n) - (\mu_1 \chi_1^n + \mu_2 \chi_2^n)(1 + M^n) \\ \gamma_{\text{pp}}(M^n) - \gamma_{\text{pd}}(M^n) - \mu_2 \chi_2^n (1 + M^n) \\ \gamma_{\text{pp}}(M^n) - \gamma_{\text{pd}}(M^n) \\ -\delta(1 + M^n) \end{pmatrix}.$$

A similar relation between $\mathbf{W}^\#$ and \mathbf{W}^{n+1} can be read from equation (3.6). Thus, assuming that $\mathbf{W}^n \geq 0$ and $S^n = 1 - \sum_i W_i^n \geq 0$ at the time t^n , the following restriction of the time step

$$\Delta t < \min \left(\frac{1}{\max_i \|\bar{\mathbf{G}}_i^n - \mathbf{F}^n\|_\infty}, \frac{1}{\|\gamma_{\text{sd}}(M^n) + \mathbf{F}^n\|_\infty} \right) := \Delta t_W. \quad (3.15)$$

ensures that $\mathbf{W}^{n+1} \geq 0$ and $S^{n+1} \geq 0$. Similarly, the forward Euler scheme in equation (3.7) and in equation (3.10) on the vascularization, leads to

$$\Delta t < \min\left(\frac{1}{\eta}, \frac{1}{\lambda}\right) := \Delta t_{\text{angio}}. \tag{3.16}$$

Finally, since the velocity might be very small, to prevent too large Δt , we arbitrarily choose a velocity \bar{v} and our CFL condition reads⁶

$$\Delta t = C_{\text{CFL}} \min\left(\frac{1}{\bar{v}} \min(\Delta x, \Delta y), \Delta t_{\text{adv}}, \Delta t_W, \Delta t_{\text{angio}}\right), \tag{3.17}$$

for a given constant $C_{\text{CFL}} < 1$.

Note that concerning the clinical cases that we deal with, we observe — thanks to easy (but technical) calculations — that there is a ratio of at least 10 between Δt_{adv} and Δt_W . Therefore, the stability condition for the set of equations (2.1)–(2.3), (2.6), (2.8), (2.14) and (2.15) is highly driven by the advection part. Therefore, it does not seem necessary to use an implicit scheme in our cases.

4. Numerical Results

4.1 Numerical tools to compare the results with the CT scans

In order to compare the numerical results to the CT scans, we have to define the appropriate quantities of interest as well as to develop a numerical tool that reproduces the grey scale.

4.1.1 *Numerical determination of the tumour area, the necrotic part and the tumour mass.* Let the threshold ϵ_{th} be the minimal fraction of tumour cells above which we define numerically the tumour. The tumour area, i.e. numerically measured, reads

$$\mathcal{A}(t) = \int_{\Omega} \mathbb{1}_{\{\mathbf{x}: P(t, \mathbf{x}) + N(t, \mathbf{x}) > \epsilon_{\text{th}}\}}(\mathbf{x}) \, d\mathbf{x}. \tag{4.1}$$

We also define the area of each cancer cell population as

$$\mathcal{A}_J(t) = \int_{\Omega} \mathbb{1}_{\{\mathbf{x}: J(t, \mathbf{x}) > \epsilon_{\text{th}}\}}(\mathbf{x}) \, d\mathbf{x}, \quad \text{for } J \in \{P_1, P_2, P_3, N\}. \tag{4.2}$$

We also define the mass of each population, and the total proliferative mass at any time as

$$\mathcal{M}_J(t) = \int_{\Omega} J(t, \mathbf{x}) \, d\mathbf{x}, \quad J \in \{P_1, P_2, P_3, N\}, \tag{4.3}$$

$$\mathcal{M}(t) = \int_{\Omega} P(t, \mathbf{x}) \, d\mathbf{x}. \tag{4.4}$$

⁶In the simulations, we choose $\bar{v} = 1$ cm/month, considering 30 days in one month and $C_{\text{CFL}} = 0.4$.

4.1.2 *Numerical reconstitution of CT scans.* The comparison of the numerical simulations with the CT scans raises an important difficulty. Actually, unlike the numerics that provide the numerical values at any point of each quantity S , P and N , the CT scans provide grey levels that are related to local radiodensities thanks to the Hounsfield scale. Since Hounsfield unit makes it possible to quantify the tumour area and to detect its location on CT scans, we introduce a numerical Hounsfield unit, which is a linear combination of the numerical results. More precisely, we consider a linear grey scale ranging from black to white. To each species (P cells, healthy cells and necrotic cells), we allocate coefficients τ_P , τ_S and τ_N , we then plot the quantity

$$\tau_P P + \tau_N N + \tau_S S, \quad (4.5)$$

which is a kind of numerical grey-level. Since for abdominal CT scans, the Hounsfield scale is limited from -200 to $+200$, we arbitrarily fix the above coefficients to

$$\tau_P = 60, \quad \tau_S = 120, \quad \tau_N = -140,$$

and we set the value -200 to black colour and $+200$ to white colour.

4.2 Extensive study of one specific patient

4.2.1 *Comparison of the numerical results with to clinical data.* We focus on Patient A for whom we have the whole clinical protocol, as well as the clinical data of the tumour area evolution and a sequence of CT scans. The numerical simulations are performed in a square of side $L = D = 6$ cm with 120 points in each direction. The time step Δt is computed by using equation (3.17).

We choose the numerical parameters in order to reproduce the evolution of the tumour area. In particular, we did not try to fit with the images, we only verify that the spatial evolution is plausible compared to the images. The parameters are summarized in Table 2.

The numerical tumour area is then compared to the measured areas on Fig. 1(g) (the circles represent the real data and the solid lines represent the numerical simulation). It is worth noting that according to this figure, the evolution of the tumour area is well reproduced. We emphasize that the initial conditions are crucial in the tumour growth. In order to match qualitatively with the shape of the lesion at the initial time (see Fig. 1(a)), the initial condition is chosen as a perturbed ellipse. More precisely, given three parameters r_1 , r_2 and e , we define in the domain Ω , $d(\mathbf{x})$ as

$$d(\mathbf{x}) = \sqrt{\left(\frac{x - L/2}{e(x - L/2) + cr_1}\right)^2 + \left(\frac{y - D/2}{e(y - D/2) + cr_2}\right)^2}, \quad (4.6)$$

with $\mathbf{x} = (x, y)$ and where $c = \frac{2\pi}{2\pi - \arccos(1 - 2\epsilon_{th})}$. The function Y defined by⁷

$$Y(\mathbf{x}) = \begin{cases} 1 & \text{if } d(\mathbf{x}) \leq 0.5, \\ 0 & \text{if } d(\mathbf{x}) \geq 1, \\ \frac{1}{2}(1 - \cos(2\pi d(\mathbf{x}))) & \text{else,} \end{cases} \quad (4.7)$$

⁷Note that if $e = 0$, then Y is rotationally invariant.

TABLE 2 List of parameters of the models and their values for the two patients considered – $d = \text{day}$

Name	Meaning	Unit	Value for fit	Value for fit
			Patient A (Fig. 1(g))	Patient B (Fig. 10(g))
γ_0	Tumour cells growth rate	d^{-1}	$2.0\text{e}-2$	$6.33\text{e}-3$
γ_1	Tumour cells apoptosis rate	d^{-1}	$8.0\text{e}-3$	$4.46\text{e}-2$
C_S	Healthy tissue apoptosis rate compared to γ_1	—	10	10
M_{th}	Hypoxia threshold	—	2	2
δ	Elimination rate of the necrotic tissue by the immune system	d^{-1}	$1.33\text{e}-2$	$8.19\text{e}-2$
ψ	Diffusion rate of the nutrients	$\text{cm}^2.\text{d}^{-1}$	$1.33\text{e}-2$	$3.33\text{e}-3$
η	Consumption rate of tumour cells	d^{-1}	$6.67\text{e}-2$	$8.05\text{e}-3$
α	Angiogenic excitability	$\text{cm}^{-1}.\text{d}^{-2}$	$1.11\text{e}-3$	$8.0\text{e}-3$
λ	Elimination rate of angiogenic growth factor signal	d^{-1}	$2.0\text{e}-2$	0.68
C_0	Angiogenic capacity of healthy tissue	d^{-1}	$3.33\text{e}-2$	$3.33\text{e}-2$
k	Tissue permeability	$\text{kg}^{-1}.\text{cm}^3.\text{d}$	1	1
T_{ini}^1	Beginning (in days) of the treatment \mathcal{T}_1 administration	d	119	0
T_{end}^1	Ending (in days) of the treatment \mathcal{T}_1 administration	d	867	845
T_{ini}^2	Beginning (in days) of the treatment \mathcal{T}_2 administration	d	867	1049
T_{end}^2	Ending (in days) of the treatment \mathcal{T}_2 administration	d	1298	1600
μ_1	Proliferative cells death rate due to treatment \mathcal{T}_1	d^{-1}	$7.17\text{e}-3$	$3.45\text{e}-3$
ν_2	Inhibition rate of the angiogenesis by treatment \mathcal{T}_2	—	0.8	0.90
μ_2	Proliferative cells death rate due to treatment \mathcal{T}_2	d^{-1}	$4.27\text{e}-3$	$3.0\text{e}-4$
ϵ_{th}	Minimal proportion of tumour cells that can be detected on scans – Minimal threshold for the numerical location of the tumour	—	$1.0\text{e}-2$	0.1
Σ_{ini}	Proportion of cells that are resistant to imatinib at the time $t = 0$ – Equivalent to $(P_2 + P_3)_{t=0}$	—	$3\text{e}-06$	0.10
q_{ini}	Proportion of imatinib resistant cells that also resist to sunitinib at time $t = 0$ – Equivalent to $(P_3/P_2)_{t=0}$	—	$7.5\text{e}-3$	0.41
ξ_{ini}	Angiogenic growth factor signal at time $t = 0$	$\text{cm}.\text{d}^{-1}$	$3.33\text{e}-3$	0
ϵ_{ξ}	Residual production of growth factor	—	0.1	0.1
L, D	Dimensions of the computational domain	cm	6	12
N_x, N_y	Number of point for each dimension of the computational domain	—	120	132
r_1	Radius along x -axis of the initial condition	cm	0.47	0.5
r_2	Radius along y -axis of the initial condition	cm	0.36	0.5
e	Kind of eccentricity of the initial condition	—	0.35	0
β	Twin-WENO5 weight	—	0	0.3

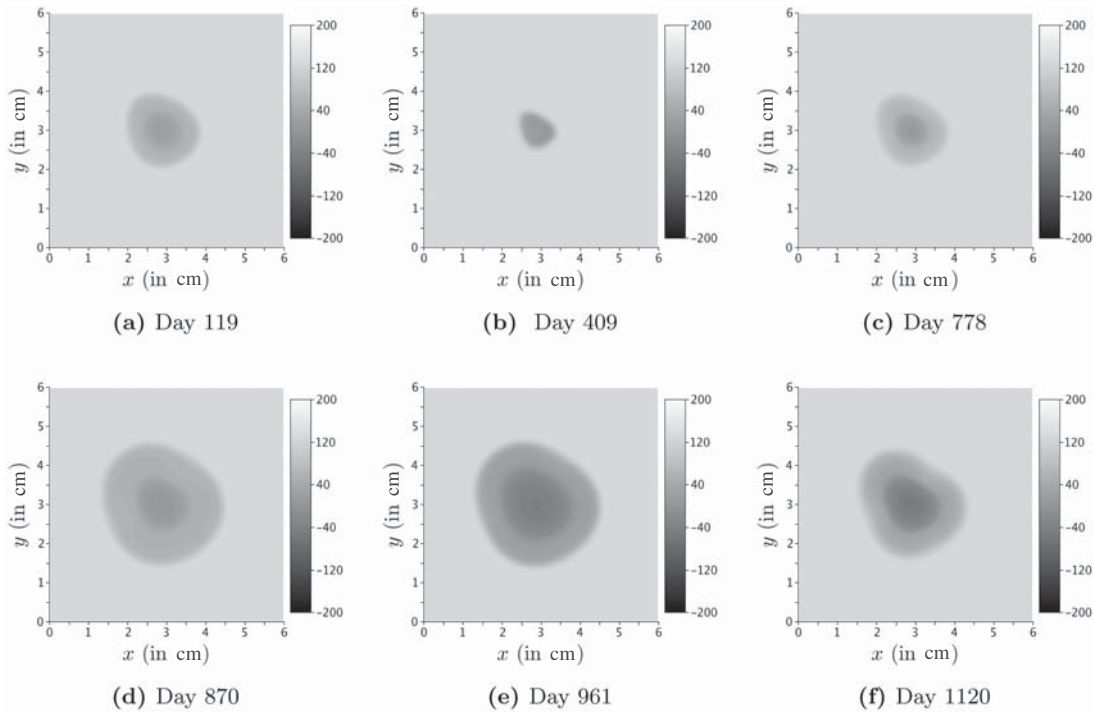


FIG. 7. Numerical simulations for Patient A: spatial evolution of the lesion with numerical reconstitution of CT scans.

is then used in order to impose the initial conditions:

$$\begin{aligned}
 P_1|_{t=0} &= (1 - \Sigma_{\text{ini}})Y, & P_2|_{t=0} &= \frac{\Sigma_{\text{ini}}}{1 + q_{\text{ini}}}Y, & P_3|_{t=0} &= q_{\text{ini}}P_2(t=0), & N|_{t=0} &= 0, \\
 M|_{t=0} &= 2M_{\text{th}},
 \end{aligned} \tag{4.8}$$

where Σ_{ini} denotes the proportion of cells that are resistant to treatment \mathcal{T}_1 and q_{ini} is the proportion of P_2 cells that resist also to treatment \mathcal{T}_2 . For Patient A, we choose $e = 0.35$ and $r_1 = 0.47$; $r_2 = 0.36$.

The spatial aspects of the numerical simulations presented in Fig. 7 make appear the following facts:

- i) During the phase without treatment, from Day 0 to Day 119, the tumour grows. Since necrotic and proliferative cells are present, the numerical tumour is heterogeneous, as reported by Fig. 7(a).
- ii) Then treatment \mathcal{T}_1 is delivered from Day 119 to Day 867. P_1 cells are killed and necrotic cells become predominant. Because of the choice of the coefficient τ_N , the numerical tumour becomes homogeneous and darker as shown by Fig. 7(b).
- iii) The rebound of the proliferative activity just before the regrowth of the tumour at Day 776 is characterized by an increase in tumour heterogeneity: a proliferative rim appears and gradually fulfil the necrotic interior of the tumour as illustrated by Fig. 7(c). It is worth noting that treatment \mathcal{T}_1 is still delivered and thus resistant cells start to be predominant.

- iv) Then treatment \mathcal{T}_2 is delivered from Day 867 to Day 1298. Once again, the necrotic population increases, and the numerical tumour is darker, as shown by Fig. 7(d,e).
- v) Finally, at Day 1116, new therapeutic failure is getting ready. It is characterized once again by a proliferative rim on the tumour boundary (see Fig. 7).

Interestingly, the numerical spatial results are in accordance with the data, at least up to the last relapse around Day 1000. Actually, the five steps that have been numerically observed are reported by CT scans (see Fig. 1(a–f)).

After Day 1116, our model is probably no longer valid since the numerical structure of the tumour is very different from the CT scan. Maybe other phenomena that are not accounted for by our model occur, such as micro-environment changes or cell mutations. Some interactions in the third direction (not accounted for here) can be also involved.

We emphasize that the model seems to provide important information that clinicians cannot have access to with imaging devices. More precisely, Fig. 8, which presents the area and mass evolution of *each* cell population, makes it possible to state that according to our model:

- During the first shrinkage of the tumour caused by treatment \mathcal{T}_1 , from Day 119 to Day 406, we observe that
 - i) Treatment \mathcal{T}_1 kills P_1 cells that become necrotic tissue.
 - ii) The reduction of the area is due to the elimination of necrotic cells by the immune system.
 - iii) P_2 and P_3 cells that are not sensitive to treatment \mathcal{T}_1 keep dividing.

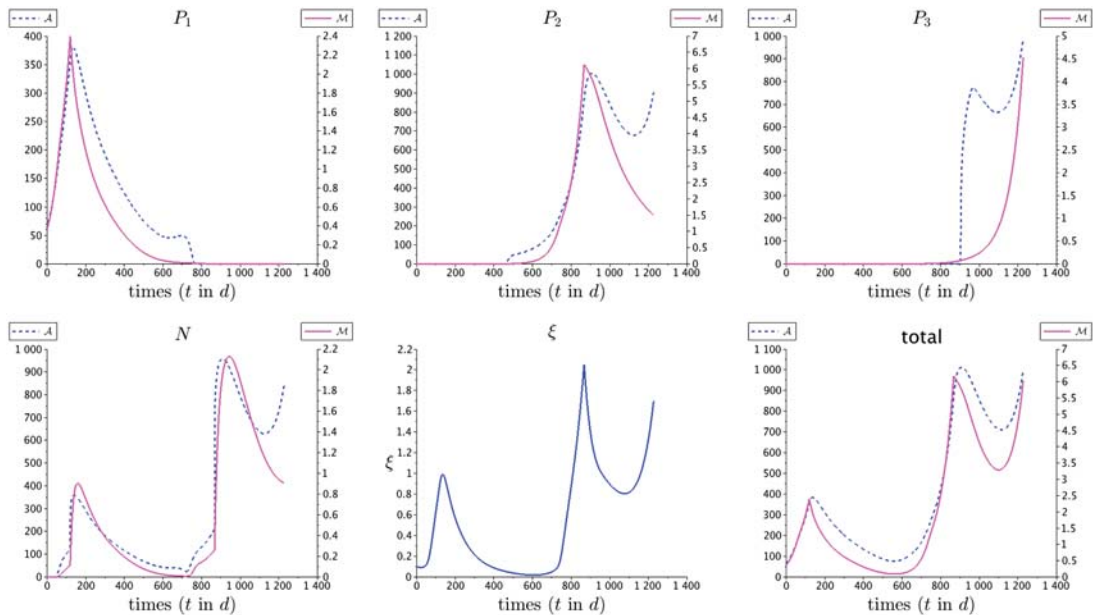


FIG. 8. Evolution of the mass (integral of grey levels, in arbitrary unit) and area (mm^2) of each cellular population and angiogenic signal evolution ($\text{cm}\cdot\text{d}^{-1}$) given by the numerical simulations.

- During few months, from Day 406 to Day 778, the tumour area continues to slowly decrease due to the death of P_1 cells; however, P_2 and P_3 cells keep growing and replace progressively the eliminated necrotic cells. Even though the cellular activity of P_2 and P_3 is not affected by the treatment, this leads in a first time, to a stabilization of the tumour area, before a regrowth of the tumour at Day 778. Actually, when $P_2 + P_3$ becomes too high, the tumour growth reoccurs, governed by cells that are resistant to treatment \mathcal{T}_1 .
- During treatment \mathcal{T}_2 , from Day 867 to Day 1298, we can notice that
 - i) P_1 cells are still sensitive to the treatment.
 - ii) P_2 cells become necrotic since they are sensitive to treatment \mathcal{T}_2 .
 - iii) P_3 cells that are resistant to the two treatments keep growing.

It is worth noting that for each relapse, the proliferative activity occurs on the tumour boundary, where there are nutrients. Moreover, our model produces differences in the evolution of the tumour area \mathcal{A} and the tumour mass evolution \mathcal{M} given, respectively, by (4.1) and (4.4).

In particular, the mass of cancer cells decreases right after the drug delivery, while the tumour area decreases with a delay in each case. This delay may be due to the fact that the killed proliferative cells turn into the necrotic phase. Therefore, the total area is still the same until the necrotic cells are eliminated by the immune system. In addition, our model distinguishes the effect on angiogenesis of the two treatments. In both cases, the angiogenic signal decreases but for different reasons. Actually, while treatment \mathcal{T}_2 inhibits directly the angiogenic signal, treatment \mathcal{T}_1 kills P_1 cells, which implies indirectly a decrease of the production of this signal.

4.2.2 Numerical study of the influence of treatment \mathcal{T}_1 efficacy. We focus now on the numerical study of different outcomes of treatment \mathcal{T}_1 to investigate their influence on the tumour growth. We take the parameters of Table 2, except that we let vary μ_1 . Let us define two characteristic durations:

- T_{PFS} , which is the progression-free survival time. It is the time duration for which the tumour is smaller (in term of area) than at the beginning of the treatment.
- T_{double} , which is the time duration for which the tumour area is below twice its initial value at the beginning of the treatment.

Note that this study is purely theoretical and cannot be used for treatment optimization since the whole evolution of the disease (including the relapse phase) is needed in order to obtain the parameters that are used for the simulation. It is therefore clear that our approach, for the time being, cannot lead to the determination of an optimal protocol, but this numerical investigation is a crucial step in addressing this important challenge.

In Fig. 9(a), we show the progression-free survival time T_{PFS} with respect to μ_1 . If μ_1 is below a threshold value μ_{th} ($\mu_{\text{th}} \sim 0.0047$ for Patient A), then the tumour growth is not stopped. For μ_1 above this threshold, T_{PFS} increases rapidly and reaches a plateau, which means that it is not necessary to increase the dose, since it has no effect on T_{PFS} .

In Fig. 9(b), we provide T_{double} . As one can see, T_{double} is not increased by the increase the dose above the threshold μ_{th} , which means once again it is not necessary to increase the drug delivery above a certain threshold value.

In Fig. 9(c), we have represented the minimum size reached by the lesion with respect to μ_1 . Note that this curve is decreasing: therefore for high values of μ_1 , the minimum of the lesion area is smaller.

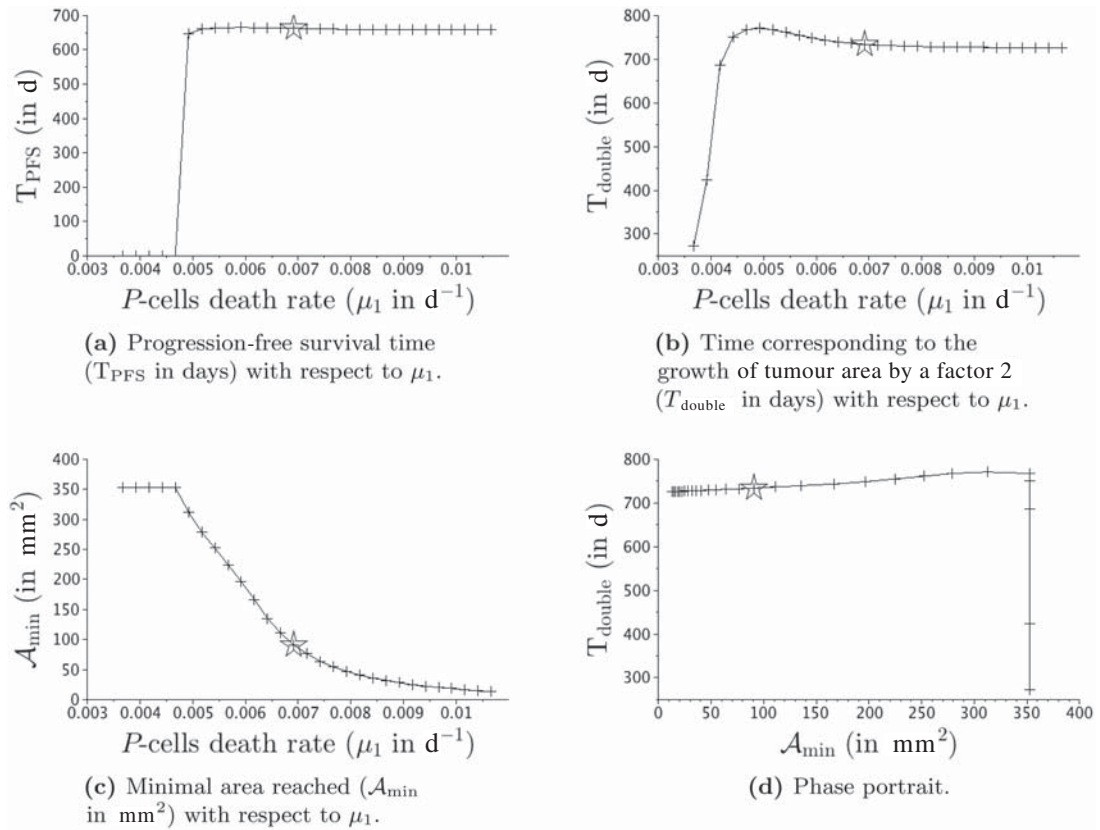


FIG. 9. Efficacy of treatment μ_1 for Patient A. The star corresponds to the parameters used in Fig. 1 for the fit of the tumour area.

However, as shown in the Fig. 9(d), the relationship between the minimum size of the lesion and the doubling time is not monotonic. In particular, if the minimum size of the lesion is very small, then the doubling time can be smaller. This could be thought of as some Darwinian selection mechanism: P_1 cells, that are predominant when the lesion is detected, are killed faster by the treatment and therefore more room and more nutrients for P_2 cells are available for their growth. Thus, the doubling time becomes smaller. These curves show that there exists a threshold μ_{th} above which treatment \mathcal{T}_1 is efficient. Beyond this threshold, the minimal tumour area decreases again, but the lifetime of the patient is not increased.

5. Discussion

In the previous section, we have extensively studied our model on one specific patient, Patient A, whose tumour lesion was followed up by a sequence of CT scans. We found parameters that make it possible to compare qualitatively the medical images with the numerics, thanks to our numerical reconstitution of CT scans, and we also fitted the tumour area. The lesion of this patient is interesting since it is confined in the inner of the liver, and thus the tumour evolution was not mechanically constrained by the organ. However, in some cases, the tumour metastasis is close to the liver boundary. In such a case, there is no

hope of providing quantitative results on the spatial evolution of the lesion, but in the next subsection, we show that the tumour area evolution can be well described.

5.1 Tumour area evolution for Patient B

In this subsection, we focus on Patient B, whose tumour evolution is quite different from Patient A. Actually, the clinical protocol of this patient was the following:

- i) Patient B was treated in a first time with a specific tyrosine kinase inhibitor (imatinib), which stabilizes the increase of the tumour area during more than 10 months before a relapse.
- ii) The multi-targeted tyrosine kinase inhibitor sunitinib was started but unlike for Patient A, it was totally inefficient.
- iii) A third treatment, was then delivered. Sorafenib is another multi-targeted tyrosine kinase inhibitor, that has both anti-angiogenic and cytotoxic effects. The tumour seemed to be sensitive to this drug during several months until the treatment failure occurs.

As illustrated by Fig. 10(g), the tumour evolution was so quick between the CT scan at Day 429 and the CT scan at Day 845 that the metastasis has reached the boundary of the liver. The boundary of the organ is clearly not included in the simulation. There is therefore no hope to provide a numerical tumour growth that would be spatially in accordance with the CT scans, since mechanical effect of the liver membrane have to be accounted for. Therefore, we focus on the tumour area as given by the clinicians, the main challenge being to capture such quick tumour growth.

Since sunitinib is totally inefficient in this case, we consider that treatment \mathcal{T}_1 is delivered from Day 0 to Day 845, while treatment \mathcal{T}_2 consists in the sorafenib, delivered from Day 1049 to Day 1600. We find parameters that make it possible to fit qualitatively the tumour area measured by the clinicians and our numerical tumour area. These parameters are given in Table 2. The initial data has been chosen rotationally invariant. As we can see, the tumour evolution is very stiff: between Day 416 and Day 614 the tumour area has been multiplied by more than 9, and once sorafenib is delivered the tumour area decreases from 4500 to 2850 mm². We manage, at least qualitatively, to obtain such behaviour, even though the fit is not perfect.

We have also investigated the efficacy of the treatment \mathcal{T}_1 , as for Patient A. It has been observed that the progression-free survival time T_{PFS} , the doubling time T_{double} and the minimum area reached by the lesion \mathcal{A}_{min} have the same profile as the patient studied in the previous section. In particular, there exists a threshold μ_{th} below which treatment has no effect on T_{PFS} . Then an increase of the dose does not improve the T_{PFS} that reached, as for Patient A, a plateau beyond μ_{th} . The doubling time T_{double} with respect to μ_1 is also not monotonic, contrary to \mathcal{A}_{min} . Thus, as previously, beyond the threshold μ_{th} , the minimal tumour area decreases again, but the overall survival time of the patient is not increased.

5.2 Consistency of the model

Our model reproduces the clinical data given for Patient A and Patient B. Moreover, it is possible to account for the following behaviours that have been reported by physicians as shown in the Fig. 11 (see Table 3 in the [Supplementary Material](#), for the different values of the used parameters):

- a) The metastasis is controlled by the treatment \mathcal{T}_1 (imatinib). In this case, there is no clinical need to change the treatment.

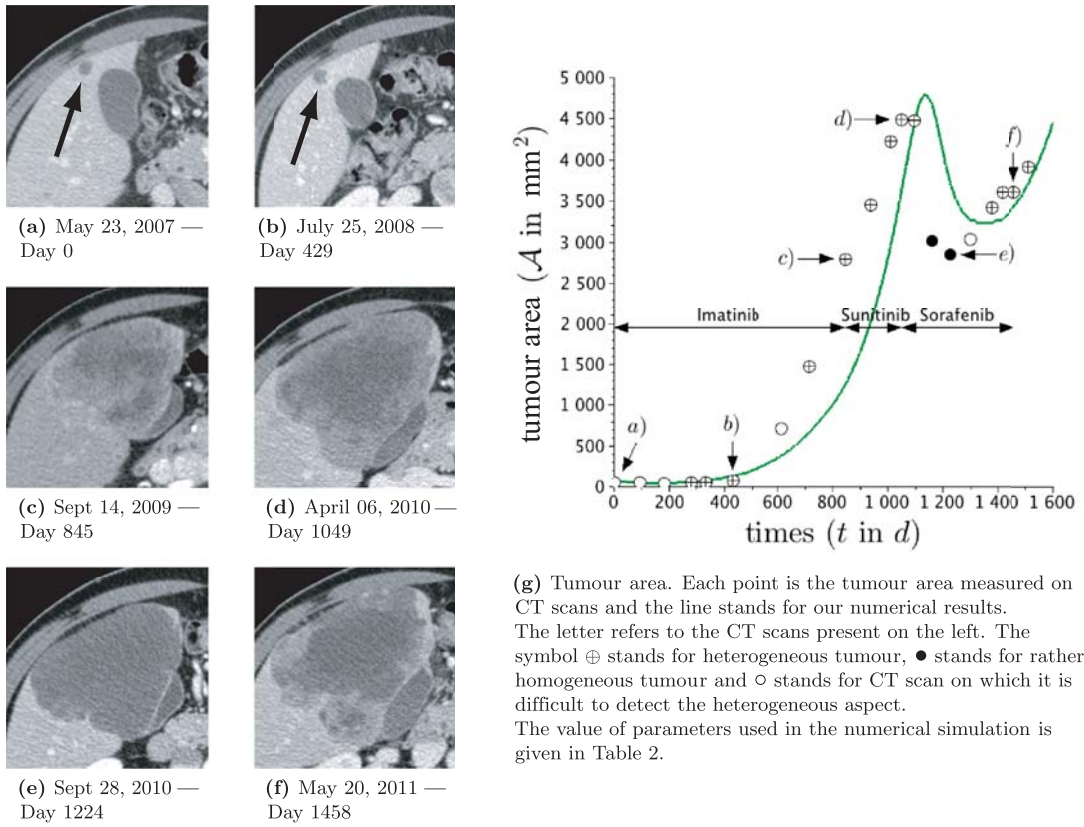


FIG. 10. Spatial evolution of the liver metastasis of Patient B on a series of CT scans. The small round lesion⁹ in the top of Fig. 10(a) is considered.

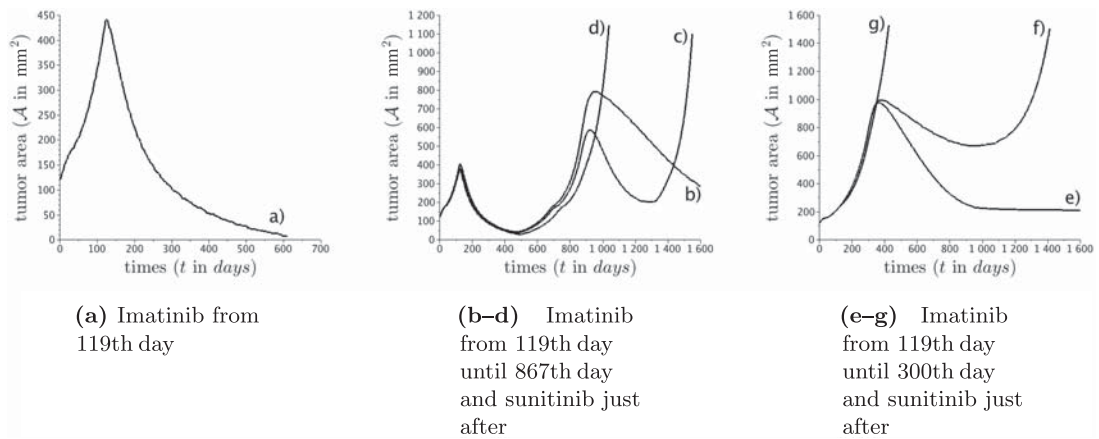


FIG. 11. Different behaviours accounted for by the model.

⁹Do not confuse the metastasis with the gallbladder that are bigger on the first two CT scans.

- b) The metastasis is controlled by the treatment \mathcal{T}_1 but then the tumour regrows. The treatment \mathcal{T}_2 (sunitinib or sorafenib) is then delivered successfully, and the tumour area is controlled.
- c) The metastasis is controlled by the treatment \mathcal{T}_1 before a first relapse. Then, the treatment \mathcal{T}_2 is efficient before a second relapse.
- d) The metastasis is controlled by the treatment \mathcal{T}_1 before a first relapse. Then, the treatment \mathcal{T}_2 is totally inefficient.
- e) The treatment \mathcal{T}_1 is totally inefficient. Then, the treatment \mathcal{T}_2 is efficient and the tumour area is controlled.
- f) The treatment \mathcal{T}_1 is totally inefficient. Then, the treatment \mathcal{T}_2 is efficient before a relapse.
- g) The treatment \mathcal{T}_1 is totally inefficient. Then, the treatment \mathcal{T}_2 is totally inefficient. This profile holds for a patient with a genetic mutation EXON, as reported by [Andersson *et al.* \(2006\)](#), or [Hirota *et al.* \(1998\)](#).

6. Conclusion

In this article, we have provided a patient-dependent model, based on PDEs, that describes the global behaviour of GIST metastasis to the liver during the different stages. We have presented the numerical methods used to solve the PDE system and we introduced a new WENO5-type scheme, called twin-WENO5. Then, this model has been numerically compared with clinical observations concerning Patient A, who have been treated successively by imatinib and sunitinib. As presented by Fig. 1(g), our model provides results that are qualitatively in accordance with the clinical data. In particular, our model is able to describe not only the evolution of the size of the lesion but also its structure, as illustrated by Figs. 1 and 2.

Interestingly, it has been reported by our simulations that a rim of proliferative cells appears on the tumour boundary just before the relapse time. This seems to be corroborated in the CT scan images by an increase of the tumour heterogeneity, in the sense of grey level, before the regrowth. The more the metastases are heterogeneous, the quicker is the relapse. This result underlines the fact that the RECIST criteria is not sufficient to evaluate the efficiency of a treatment.

We also investigated numerically the effect of the parameter μ_1 , linked to the efficacy of treatment \mathcal{T}_1 . We have shown that, according to the numerical model, increasing the value of μ_1 , which can be seen as an increase in the drug delivery, does not provide better results in terms of progression-free survival time as reported by Fig. 9.

It is worth noting that our model fits well with the data, although it is not predictive. Indeed, as explained in Fig. 11(b–d), one can see that the three typical behaviours b–d are the same during the first 400 days. However, their later behaviour are quite different. It is therefore not possible to predict the evolution of a solution knowing only its behaviour during this first part. In other words, one can find different sets of parameters that give the same initial behaviour of the tumour but that will lead to drastically different long-term evolution. This means that more precise data such as functional imaging data could be necessary for a better analysis of the inner structure of metastases.

In conclusion, we have provided a model that fits with the clinical CT scans we had. The forthcoming work will consist in adding more biological information that cannot be obtained from the CT scans, in order to provide a predictive model. Note that functional imaging data (TEP or MRI) or biopsies might be crucial in enriching the present model.

Acknowledgements

The medical data used in this article have been provided to the authors by the Institut Bergonié, F-33000, Bordeaux, France. We thank the Institut Bergonié for its collaboration and particularly the oncologist MD Binh Bui. We also thank very warmly Dr H. Fathallah-Shaykh for discussions and advice that significantly contributed to improving the quality of this article.

Funding

This study has been carried out within the frame of the LABEX TRAIL, ANR-10-LABX-0057 with financial support from the French State, managed by the French National Research Agency (ANR) in the frame of the ‘Investments for the future’ Programme IdEx (ANR-10-IDEX-03-02).

Experiments presented in this article were carried out using the PlaFRIM experimental testbed, being developed under the Inria DIHPES development action with support from LABRI and IMB and other entities: Conseil Régional d’Aquitaine, FeDER, Université de Bordeaux and CNRS (see <https://plafrim.bordeaux.inria.fr/>).

This work was partially supported by Associative Research Program (PIA) from Conicyt under grant number FB0001 (to P.C.) and by Universidad del Bio-Bio under grant DIUBB 121909 GI/C and DIUBB 122109 GI/EF (to P.C.).

Supplementary material

Supplementary material is available at <http://imammb.oxfordjournals.org>.

REFERENCES

- AMBROSI, D. & PREZIOSI, L., (2002) On the closure of mass balance models for tumor growth. *Math. Models Methods Appl. Sci.*, **12**, 737–754.
- ANDERSSON, J., BUMMING, P., MEIS-KINDBLOM, J. M., SIHTO, H., NUPPONEN, N., JOENSUU, H., ODEN, A., GUSTAVSSON, B., KINDBLOM, L. G. & NILSSON, B. (2006) Gastrointestinal stromal tumors with kit exon 11 deletions are associated with poor prognosis. *Gastroenterology*, **130**, 1573–1581.
- BENZEKRY, S., LAMONT, C., BEHESHTI, A., TRACZ, A., EBOS, J. M., HLATKY, L., & HAHNFELDT, P. (2014). Classical mathematical models for description and prediction of experimental tumor growth. *PLoS Comput. Biol.*, **10**, e1003800.
- BILLY, F., RIBBA, B., SAUT, O., MORRE-TROUILHET, H., COLIN, T., BRESCH, D., BOISSEL, J.-P., GRENIER, E. & FLANDROIS, J.-P. (2009) A pharmacologically based multiscale mathematical model of angiogenesis and its use in investigating the efficacy of a new cancer treatment strategy. *J. Theor. Biol.*, **260**, 545–562.
- BLAY, J. Y. (2011) A decade of tyrosine kinase inhibitor therapy: historical and current perspectives on targeted therapy for GIST. *Cancer Treat. Rev.*, **37**, 373–384.
- BLAY, J. Y., LE CESNE, A., CASSIER, P. A. & RAY-COQUARD, I. L. (2012) Gastrointestinal stromal tumors (GIST): a rare entity, a tumor model for personalized therapy, and yet ten different molecular subtypes. *Discov. Med.*, **13**, 357–67.
- BRESCH, D., COLIN, T., GRENIER, E., RIBBA, B. & SAUT, O. (2009) A viscoelastic model for avascular tumor growth. *Discrete Continuous Dyn. Syst.*, 101–108.
- BRESCH, D., COLIN, T., GRENIER, E., RIBBA, B. & SAUT, O. (2010) Computational modeling of solid tumor growth: The avascular stage. *SIAM J. Sci. Comput.*, **32**, 2321–2344.
- BYRNE, H. & PREZIOSI, L. (2003) Modelling solid tumor growth using the theory of mixtures. *Math. Med. Biol.*, **20**, 341–366.

- COLIN, T., GALLINATO, O., POIGNARD, C. & SAUT, O. (2014) Tumor growth model for ductal carcinoma: from in situ phase to stroma invasion. Submitted Report RR-8502, INRIA.
- COLIN, T., IOLLO, A., LOMBARDI, D. & SAUT, O. (2012) System identification in tumor growth modeling using semi-empirical eigenfunctions. *Math. Models Methods Appl. Sci.*, **22**, 1250003.
- DEMATTEO, R. P., LEWIS, J. J., LEUNG, D., MUDAN, S. S., WOODRUFF, J. M. & BRENNAN, M. F. (2000) Two hundred gastrointestinal stromal tumors: recurrence patterns and prognostic factors for survival. *Ann. Surg.*, **231**, 51.
- HIROTA, S., ISOZAKI, K., MORIYAMA, Y., HASHIMOTO, K., NISHIDA, T., ISHIGURO, S., KAWANO, K., HANADA, M., KURATA, A., MUHAMMAD TUNIO, G., MATSUZAWA, Y., KANAKURA Y., SHINOMURA, Y. & KITAMURA, Y. (1998) Gain-of-function mutations of c-kit in human gastrointestinal stromal tumors. *Science*, **279**, 577–80.
- HOLMES, K., LL, O., ROBERTS, A. M., THOMAS, & CROSS, M. J. (2007) Vascular endothelial growth factor receptor-2: Structure, function, intracellular signalling and therapeutic inhibition. *Cell. Signal.*, **19**, 2003–2012.
- LIU, X. D., OSHER, S. & CHAN, T. (1994) Weighted essentially non-oscillatory schemes. *J. Comput. Phys.*, **115**, 200–212.
- LORZ, A., LORENZI, T., CLAIRAMBAULT, J., ESCARGUEIL, A. & PERTHAME, B. (2013) Effects of space structure and combination therapies on phenotypic heterogeneity and drug resistance in solid tumors. *arXiv preprint arXiv:1312.6237*.
- NILSSON, B., BUMMING, P., MEIS-KINDBLOM, J. M., ODEN, A., DORTOK, A., GUSTAVSSON, B., SABLINSKA, K. & KINDBLUM, L. G. (2005) Gastrointestinal stromal tumors: the incidence, prevalence, clinical course, and prognostication in the preimatinib mesylate era—a population-based study in western sweden. *Cancer*, **103**, 821–9.
- RIBBA, B., SAUT, O., COLIN, T., BRESCH, D., GRENIER, E. & BOISSEL, J. P. (2006) A multiscale mathematical model of avascular tumor growth to investigate the therapeutic benefit of anti-invasive agents. *J. Theor. Biol.*, **243**, 532–541.
- SAUT, O., LAGAERT, J-B., COLIN, T. & FATHALLAH-SHAYKH, H. (2014) A multilayer grow-or-go model for GBM: effects of invasive cells and anti-angiogenesis on growth. *Bull. Math. Biol.*, **76**, 2306–2333.
- SCHRAMM, N., ENGLHART, E., SCHLEMMER, M., HITTINGER, M., ÜBLEIS, C., BECKER, C. R., REISER, M. F. & BERGER, F. (2013) Tumor response and clinical outcome in metastatic gastrointestinal stromal tumors under sunitinib therapy: comparison of recist, choi and volumetric criteria. *Eur. J. Radiol.*, **82**, 951–958.
- SUZUKI, C., JACOBSSON, H., HATSCHEK, T., TORKZAD, M. R., BODÉN, K., ERIKSSON-ALM, Y., BERG, E., FUJII, H., KUBO, A. & BLOMQUIST, L. (2008) Radiologic measurements of tumor response to treatment: practical approaches and limitations I. *Radiographics*, **28**, 329–344.